sustainability

MDPI

Article

A Physically Consistent Modeling Framework for Evaluating Dust Aerosol Direct Radiative Forcing on Cotton GPP and Yield in Arid Oases

Kexin Li [1,2], Nurmemet Erkin [1,*], Xarapat Ablat [3], Hongqi Wu [1,2,*], Ababaikere Maimaiti [4], Xiangge Wang [1,2] and Yuwei Li [1,2]

1 College of Resources and Environment, Xinjiang Agricultural University, Urumqi 830052, China; 320243730@stu.xjau.edu.cn (K.L.); 320243751@stu.xjau.edu.cn (X.W.); 320233718@xjau.edu.cn (Y.L.)
2 Xinjiang Engineering Technology Research Center of Soil Big Data, Urumqi 830052, China
3 School of Engineering, Guangzhou Nanfang University, Guangzhou 510970, China; xiarepatiabulaiti@nfu.edu.cn
4 College of Computer and Information Engineering, Xinjiang Agricultural University, Urumqi 830052, China; noor@xjau.edu.cn
* Correspondence: 12514082@zju.edu.cn (N.E.); whq@xjau.edu.cn (H.W.)

Abstract

Quantifying dust aerosol radiative impacts on crop growth in arid regions is challenging due to sparse ground observation networks for photosynthetically active radiation (PAR). Conventional meteorological stations only provide regional-averaged solar radiation and fail to capture fine spatial heterogeneity and instantaneous attenuation caused by dust storms. To address this gap, this study developed a coupled framework integrating WRF-Chem, LibRadtran, multi-source remote sensing, and interpretable machine learning. We combined field sampling data, remote sensing products, and atmospheric simulations to explore how dust aerosol direct radiative forcing alters cotton gross primary productivity (GPP) and yield across the Weigan River Basin, Xinjiang, China. Results revealed significant PAR reduction induced by dust in 87% of cotton fields ($p < 0.05$). Dust presented a dual effect: it reduced photosynthetic productivity via radiation attenuation, while alleviating heat stress above 35 °C. SHAP analysis demonstrated that cotton GPP and yield declined nonlinearly when daily PAR loss exceeded 20 W·m^{-2}, with the flowering-to-boll stage (July–August) identified as the most sensitive phenological window. This study verifies the necessity of combining atmospheric models and remote sensing for fine-scale assessment of dust radiative effects in data-scarce regions. The identified threshold provides practical references for targeted field management in arid cotton areas.

Keywords: dust aerosol; direct radiative forcing; photosynthetically active radiation; gross primary productivity; cotton yield; arid oasis; atmospheric simulation

Academic Editor: Rafal Przekop

Received: 15 June 2026
Revised: 13 July 2026
Accepted: 15 July 2026
Published: 21 July 2026

1. Introduction

Global cash crop production sustainability and the stability of the ecological environmaent constitute core concerns for the international community [1–3]. Atmospheric aerosols, acting as a critical environmental stressor, have become a key constraint on global food security due to their profound impacts on crop growth. Within this broader context, the Weigan River Basin is an important agricultural oasis and high-quality cotton production base in southern Xinjiang, which plays a key role in regional food security and the development of the cotton industry. Although the region has sufficient light and a mature irrigation system, it is close to the Taklimakan Desert, with a fragile ecological environment and frequent sandstorms [4,5]. In addition to causing direct physical damage to crops, dust aerosols can also scatter and absorb solar radiation, weaken the photosynthetically active radiation (PAR) reaching the canopy, thereby reducing photosynthetic efficiency, inhibiting biomass accumulation, and ultimately limiting yield, making sandstorms the main environmental factor threatening the sustainable production of cotton and the stability of oases [6].

Dust aerosols change the surface radiation balance through direct radiative forcing. Suspended particulate matter will scatter and absorb incident solar radiation, greatly reducing PAR (400–700 nm) [7]. PAR is the only energy source for photosynthesis and also a key driving factor of gross primary productivity (GPP) and yield [8]. Therefore, the continuous attenuation of PAR under dust conditions will reduce light use efficiency, weaken carbon assimilation, and inhibit GPP, which is an important meteorological stress factor faced by crops in arid oases.

Multi-source remote sensing and machine learning are the current mainstream technical means for crop mapping, growth monitoring, and yield estimation [9]. High-resolution satellite data (such as Sentinel, Landsat) can provide continuous spectral and phenological information and can realize accurate crop classification and yield inversion when combined with algorithms such as Random Forest (RF) and Extreme Gradient Boosting (XGBoost) [10]. Coupling the WRF-Chem atmospheric model with the LibRadtran radiative transfer model can provide a physical basis for simulating the evolution of dust aerosols and their impact on surface radiation [11]. This integrated framework of "remote sensing-machine learning-model simulation" can simultaneously capture the spatial heterogeneity of crops and the radiative transfer mechanism and outperform traditional statistical methods in analyzing the aerosol-radiation-vegetation interaction [12].

In recent decades, the frequency of compound extreme events involving heatwaves and dust storms has increased markedly in the Taklamakan Desert region, which directly borders the Weigan River Basin. Liu et al. [13] reported that from 1993 to 2022, heatwave frequency and intensity in the Taklamakan Desert increased at rates of 0.21 days year^{-1} and 0.02 °C year^{-1}, respectively, with more than 40% of heatwaves accompanied by dust events that significantly lagged behind the heatwaves. Mechanistically, higher air temperatures lead to hotter and drier soils, thereby facilitating greater dust emissions and creating a positive feedback loop between heat extremes and dust outbreaks. This escalating compound hazard poses growing threats to the socioeconomic and ecological security of the surrounding oasis agricultural systems, yet the specific impacts of such compound events on cotton productivity remain critically understudied.

Despite these advances, three critical limitations persist in the current literature, which constrain the mechanistic understanding of dust impacts on agricultural productivity in arid oases. First, while numerous studies have characterized the spatiotemporal distribution of dust aerosols and their radiative forcing using atmospheric models such as WRF-Chem and LibRadtran [7,11,14,15], such studies have predominantly focused on climatic or atmospheric perspectives. In contrast, quantitative analyses of dust-induced PAR attenuation on the yields of specific economic crops—particularly cotton, the dominant cash crop in arid oases—remain remarkably scarce. The spatial heterogeneity of radiation stress and its direct linkage to crop productivity at the field scale have not been adequately quantified [16]. Second, existing crop growth models and statistical assessments commonly assume a linear or near-linear relationship between radiation reduction and yield [17,18], overlooking the possibility of critical physiological thresholds. More critically, dust radiative forcing and extremely high temperatures frequently coincide during cotton's flowering and boll-forming periods in arid regions, yet few integrated analyses have quantified their interactive effects. Whether dust-induced shading partially alleviates heat stress or exacerbates light-limited yield loss remains unresolved [19,20]. Third, although machine learning algorithms such as Random Forest and XGBoost have been widely adopted for crop mapping and yield estimation [9,10], the application of explainable artificial intelligence tools to disentangle aerosol radiative forcing from mixed environmental covariates remains underexplored in agro-environment research. Decomposition algorithms built on tree-based explainers can effectively isolate independent predictive signals from complex confounding backgrounds, providing a mature analytical paradigm for distinguishing individual stress factors [21]. This methodological gap limits the interpretability of black-box models and hinders the identification of actionable stress thresholds for field management. These knowledge gaps are particularly significant for arid oasis agriculture, where radiation limitation and heat stress frequently co-occur during critical cotton growth stages, and where precise agronomic decision-making requires not only prediction accuracy but also mechanistic interpretability. To fill this research gap, this study constructs an integrated analysis framework integrating high-resolution remote sensing, atmospheric simulation, and machine learning to quantitatively analyze the above processes at the field scale. The whole research flow is divided into three independent but interconnected functional modules for sequential calculation and result output, a modularized analytical architecture that has been proven efficient for multi-condition batch simulation and automatic result visualization in multi-disciplinary modeling research [22]: (1) Fuse multi-temporal multi-source remote sensing data (Sentinel, HLS, MODIS) with machine learning algorithms (Random Forest, XGBoost), realize high-precision cotton mapping and yield estimation using multi-dimensional features, and complete accurate spatial extraction and quantitative yield inversion. (2) Couple the WRF-Chem atmospheric model with LibRadtran, simulate the dust emission and transport processes, systematically compare the PAR under dust-free and dust scenarios, and quantify the spatiotemporal dynamics of dust aerosols and their radiative effects. (3) Adopt pixel-level spatial correlation analysis combined with the SHAP interpretable framework, quantify the contribution of PAR attenuation to cotton GPP and final yield, identify the key radiative stress threshold and the most sensitive phenological window, and evaluate the overall constraint effect and spatial heterogeneity of dust radiative forcing on regional cotton production.

2. Materials and Methods

2.1. Technical Framework

The study employs a systematic technical framework that integrates multi-source remote sensing, atmospheric modeling, and machine learning to evaluate the impact of dust aerosol direct radiative forcing on cotton gross primary productivity (GPP) and yield. The framework comprises four interconnected modules: data collection and preprocessing, cotton spatial mapping and yield estimation, dust aerosol and photosynthetically active radiation (PAR) simulation, and impact assessment of dust-induced radiation stress on cotton productivity. Figure 1 provides a graphical overview of the overall workflow and the relationships among these modules.

2.2. Study Area

The Weigan River Basin (40°57′00″–42°23′24″ N, 80°37′48″–83°31′12″ E) is located in Aksu Prefecture, Xinjiang Uygur Autonomous Region, China [2]. It originates from the continental glacier system of Khan Tengri Peak at the southern foot of the Tianshan Mountains, with a total area of about 72,400 km^2, and its administrative scope covers Baicheng, Kuqa, Xinhe, Shaya, and other counties and cities (Figure 2). The study area belongs to a typical warm temperate zone with an extremely arid continental climate, with a multi-year average temperature of 10.5 °C~11.4 °C, extremely low annual average precipitation of only 50.5~66.5 mm, and extremely high annual potential evapotranspiration of up to 2000.7 mm~2092.0 mm.

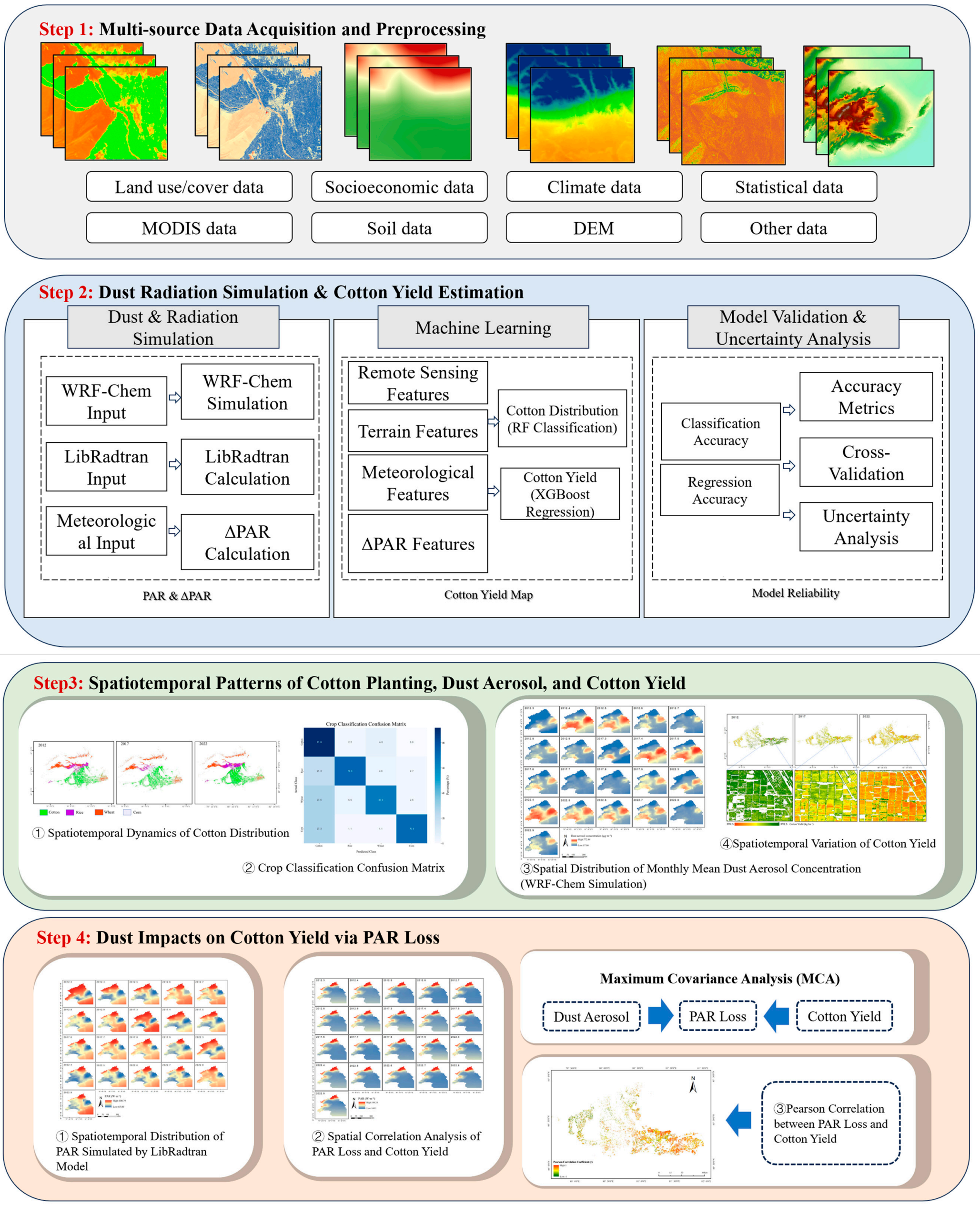

Figure 1. This study adopts a systematic technical route, which includes 4 core modules: data collection and preprocessing, cotton spatial mapping and yield estimation, dust aerosol and photosynthetically active radiation (PAR) simulation, and impact assessment of dust radiation effect on cotton productivity.

The basin sits on the northern periphery of the Taklimakan Desert, where dust aerosols are primarily generated by natural wind erosion from mobile dunes and alluvial deposits in the southern and southeastern Tarim Basin. Minor local dust emissions originate from desert-oasis ecotone degradation driven by overgrazing, irrational irrigation, and land reclamation. Regional dust is dominated by mineral oxides, including SiO_2, Al_2O_3, CaO, Fe_2O_3, MgO, and K_2O, consistent with the geochemical characteristics of arid desert dust across Central Asia [4,23]. Three dominant soil types are widely distributed throughout the watershed: Gray Desert Soil (Calcic Gypsisols), Sierozem (Calcic Cambisols), and Irrigated Warped Soil (Anthrosols). Oasis farmland soils are loam to silt loam, with sand fractions of 35–50%, silt of 30–45%, and clay of 10–20%. These loose, sand-rich topsoils are highly susceptible to wind erosion in spring after winter soil moisture depletion, providing abundant erodible materials for dust emission [7].

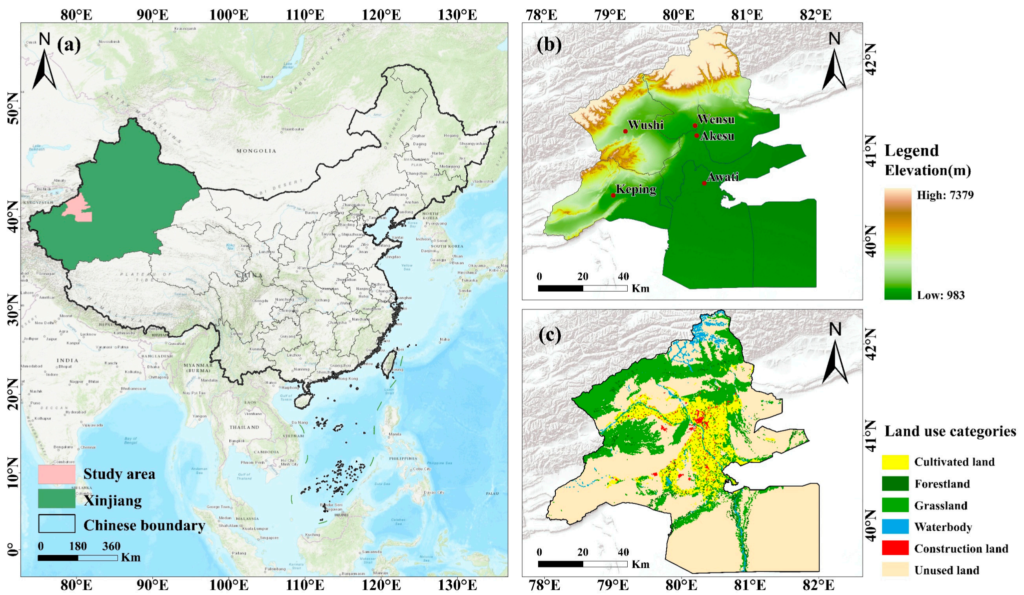

Figure 2. Geographical overview of the Weigan River Basin: (**a**) location of the study area in Xinjiang, China; (**b**) topographic gradient from the Tianshan Mountains to the Taklimakan Desert; (**c**) spatial distribution of main rivers, county boundaries, and oasis agricultural areas.

2.3. Data Collection and Preprocessing

2.3.1. Satellite Remote Sensing Data

This study uses multi-source, multi-temporal satellite remote sensing data, including Sentinel-2 multispectral images, Sentinel-1 SAR data (for VV/VH polarization backscattering) [8], HLS fusion products (for multi-source optical data consistency and high-temporal-resolution surface reflectance time series), Landsat 8 images, MODIS data (for vegetation index time series, 1 km-resolution land surface temperature and GPP), and GLC_FCS30D 30 m land cover dataset (for cultivated land mask, resampled to the study's unified resolution) [24]. All data underwent standardized preprocessing, including radiometric calibration, atmospheric correction via the 6S model, cloud masking using QA bands and Sen2Cor, mosaicking, and cropping. From preprocessed reflectance data, vegetation indices (NDVI, EVI, NDWI, NDRE) were calculated to construct a high-dimensional remote sensing feature space [25,26]. NDWI was included to characterize crop water status, as cotton is highly sensitive to water stress during its flowering and boll-forming stages [26], while NDRE was incorporated because its sensitivity to chlorophyll content and nitrogen status makes it a powerful indicator for cotton yield estimation. For Sentinel-1 SAR data, VV and VH polarization backscattering coefficients were extracted to complement optical vegetation indices, particularly for areas affected by cloud cover or dust aerosol contamination, as SAR backscatter from cotton fields exhibits distinct temporal patterns that facilitate crop discrimination. Radiometric and atmospheric corrections were performed using the FLAASH module in ENVI 5.6 for Landsat series imagery. The TOA reflectance was converted to standard surface reflectance. The mid-latitude summer atmospheric model and rural aerosol model were adopted, and the atmospheric visibility was set to 40 km according to local meteorological observations. For the 6S model, key input parameters included: mid-latitude summer atmospheric profile, rural aerosol model, atmospheric visibility of 40 km, target elevation of approximately 1000 m, and sensor altitude of 705 km for Landsat 8. For Sentinel-2 data, cloud and cloud shadow masking was performed using the Sen2Cor processor (version 2.10), with the enhanced cloud shadow algorithm enabled and a 3×3 pixel filter kernel applied for artifact reduction [27].

2.3.2. Atmospheric and Meteorological Data

The atmospheric and meteorological input data of this study come from a multi-source combination of model simulations, reanalysis datasets, and ground observations. The core data sources include the simulation results of the WRF-Chem atmospheric chemistry coupled model, the ERA5-Land high-resolution land surface reanalysis dataset, the MERRA-2 global reanalysis dust product, and the observation data of the Aerosol Robotic Network (AERONET) [28]. The WRF-Chem simulation configuration is used to simulate the processes of dust emission, transmission and deposition in the study area, and the output focuses on key optical parameters, such as dust concentration and aerosol optical depth (AOD) [11]. Continuous time series meteorological variables such as temperature, precipitation, wind speed, and specific humidity come from the ERA5-Land dataset, the MERRA-2 dust product is used for spatial comparison with the WRF-Chem output results, and the high-precision long-term AOD observation data of AERONET ground stations are used for point-scale verification and error analysis. Daily meteorological and dust concentration station data were spatially interpolated over the study area using the ordinary Kriging method in ArcGIS Pro 3.1. A spherical semi-variogram model was applied, with the number of neighboring sampling points set to 12 to guarantee interpolation reliability. The fitted spherical model yielded an average coefficient of determination (R^2) of 0.87 against the empirical semi-variogram. Leave-one-out cross-validation produced mean absolute errors of 0.31 °C for temperature, 2.8 mm for precipitation, and 18.6 $\mu g \cdot m^{-3}$ for dust concentration, confirming the reliability of the interpolation.

2.3.3. Field Survey Data

Crop type reference data were obtained by ground survey combined with visual interpretation of historical high-resolution images. Field sampling was conducted during the 2022 and 2023 cotton growing seasons (July–October), targeting key phenological periods. A handheld GPS device was used to record the geographic coordinates of the center of representative fields (positioning accuracy < 3 m), and crop types were identified in situ. For image interpretation, contemporaneous Google Earth high-resolution historical images were used, and samples were obtained by manually delineating pure pixels. A total of 1033 valid sample points were collected in this study, covering 5 types of land cover: cotton, rice, wheat, corn and others, each type was assigned a numerical label (0: others, 1: cotton, 2: rice, 3: wheat, 4: corn) for subsequent model processing, and the statistical quantity of each crop type is shown in Table 1.

Table 1. Number of field surveys and Google Earth samples for each crop type.

Crop Type	Number of Field Samples	Number of Google Earth Samples	Total
Cotton	125	252	377
Wheat	42	110	154
Rice	40	70	110
Maize	64	120	184
Others	151	59	210

To obtain accurate ground-truth data of cotton yield, this study adopts a stratified random sampling strategy to ensure that the samples can represent cotton fields under different soil types, irrigation methods, and management measures in the watershed, so as to reflect the spatial heterogeneity of yield. The data are collected by means of farmer questionnaires combined with standardized field sampling, and the standardized sampling is carried out in accordance with the established agrometeorological regulations. During the boll opening period, at least three 1 m^2 quadrats are set up in each selected cotton field, and the sampling mode adopts the three-point sampling method or the diagonal sampling method. The number of effective plants and the number of bolls per plant in each quadrat are recorded, open cotton bolls are harvested, dried to constant weight, and then weighed to determine the average single boll weight. The theoretical seed cotton yield per unit area (Y, kg ha^{-1}) is calculated by the following formula:

$$Y = D \times N \times W \times 10 \quad (1)$$

where D is planting density (plants·m^{-2}), N is the average number of bolls per plant, and W is the average weight per boll (g). The coefficient 10 is the unit conversion factor, since 1 g·m^{-2} = 10 kg·ha^{-1}.

The yield data obtained by this standardized method is used to calibrate and supplement the self-reported yield from farmer surveys, and the two together constitute a reliable ground truth dataset containing 348 measured yield records. Subsequently, the dataset is randomly divided into a training set and an independent validation set, which are respectively used for parameter training of the XGBoost model and final evaluation of prediction accuracy.

After the collection and preprocessing of all data mentioned above, detailed information on data sources and specifications used in this study is provided in Table S1 in the Supplementary Materials.

2.4. Research Methods

2.4.1. Dust Aerosol Simulation Based on WRF-Chem

To quantitatively characterize the direct radiative forcing effect of dust aerosols, this study adopts the Weather Research and Forecasting model coupled with the Chemistry module (WRF-Chem) to simulate the spatiotemporal evolution process of dust concentration in the Weigan River Basin. The simulation adopts a double nested grid configuration, and initial conditions and boundary conditions are provided by the ERA5 reanalysis dataset. The GOCART (Goddard Chemistry Aerosol Radiation and Transport) scheme is selected to parameterize the dust emission process, while the comprehensive effects of soil erodibility and near-surface wind speed are considered [14,29,30]. Detailed model configuration parameters, including domain settings, physics options, chemistry options, and dust optical properties, are provided in Table S2. As a fully online coupled meteorological chemistry model, WRF-Chem is a mainstream tool for dust aerosol simulation, and its core lies in the two-way feedback between the meteorological field and aerosol processes. Studies usually adopt dust emission parameterization schemes such as GOCART (Goddard Chemistry Aerosol Radiation and Transport) and calculate emission flux in real time in combination with surface type, soil moisture, and near-surface wind speed. This model can finely depict the complete life cycle of atmospheric dust, including transmission, diffusion, mixing, and dry and wet deposition processes. Particularly importantly, WRF-Chem can simulate dust-radiation interaction (scattering and absorption of solar radiation) and dust–cloud interaction (as cloud condensation nuclei regulate cloud microphysical processes), thereby improving the fidelity of studies related to dust storm dynamics and regional climate impacts. Subsequently, the simulated aerosol optical properties are taken as input parameters of the LibRadtran radiative transfer model, and the DISORT (Discrete Ordinates Radiative Transfer) solver is adopted to calculate the surface downward PAR under two different scenarios of a dust-free atmosphere and a dust-containing atmosphere, respectively. Then the difference in surface PAR under the two scenarios is defined as the direct dust radiative effect (ΔPAR), which is used to quantitatively evaluate the inhibitory effect of radiation attenuation caused by dust on cotton photosynthesis. The calculation formula of ΔPAR is as follows:

$$\Delta \boldsymbol{PAR} = \boldsymbol{PAR_{clean}} - \boldsymbol{PAR_{dust}} \tag{2}$$

where $\boldsymbol{PAR_{clean}}$ is the surface downward PAR under a dust-free scenario (W·m^{-2}), $\boldsymbol{PAR_{dust}}$ is the surface downward PAR under a dust-containing scenario (W·m^{-2}), and $\Delta\boldsymbol{PAR}$ represents the PAR loss caused by dust aerosols. A negative $\Delta\boldsymbol{PAR}$ represents radiation attenuation, and the larger the absolute value is, the stronger the radiative forcing effect is.

2.4.2. PAR Calculation Based on LibRadtran

This study adopts the radiative transfer model library (LibRadtran) coupled with the DISORT solver to calculate the downward PAR under two atmospheric scenarios of dust-free and dust-containing [31]. The PAR difference under the two scenarios is taken as the radiation attenuation caused by dust, and the relationship between radiation attenuation and dust concentration is further explored by correlating this difference with dust aerosol optical depth (AOD). Detailed radiative transfer configuration parameters are provided in Table S3. The PAR attenuation rate caused by dust is calculated by the following supplementary formula:

$$\boldsymbol{\eta} = \frac{\Delta\boldsymbol{PAR}}{\boldsymbol{PAR_{clean}}} \times 100\% = \frac{\boldsymbol{PAR_{clean}} - \boldsymbol{PAR_{dust}}}{\boldsymbol{PAR_{clean}}} \times 100\% \tag{3}$$

where $\boldsymbol{\eta}$ represents the PAR attenuation rate (%) directly caused by dust aerosols, which can intuitively reflect the weakening effect of dust on PAR. The definitions of variables $\Delta\boldsymbol{PAR}$, $\boldsymbol{PAR_{clean}}$, and $\boldsymbol{PAR_{dust}}$ are consistent with those described in Section 2.4.1. The calculated $\boldsymbol{\eta}$ can directly reflect the net reduction in photosynthetically active radiation caused by the scattering and absorption of dust aerosols and is the core index for evaluating the impact of radiation stress on cotton photosynthesis.

2.4.3. Cotton Planting Area Mapping Based on Random Forest

This study constructs a multi-dimensional feature set including multi-temporal remote sensing vegetation indices, topographic factors, and meteorological variables, and then adopts the Random Forest classification algorithm to automatically extract the spatial distribution of cotton planting in the Weigan River Basin. In the model construction stage, all labeled samples are divided into a training set and a test set according to the ratio of 8:2 [32]. The training set is used to train the model and optimize parameters, and the independent test set is used for accuracy verification. Five indicators, including Overall Accuracy, Kappa coefficient, Producer's Accuracy, User's Accuracy, and F1-score, are adopted to comprehensively evaluate the classification effect. The multi-dimensional evaluation ensures the accuracy and reliability of the extracted cotton planting areas and provides a reliable spatial data basis for subsequent yield estimation and impact analysis. Among them, F1-score integrates precision and recall, and its calculation formula is as follows:

$$\boldsymbol{F}1 = 2 \times \frac{\boldsymbol{Precision} \times \boldsymbol{Recall}}{\boldsymbol{Precision} + \boldsymbol{Recall}} \tag{4}$$

where Precision (i.e., User's Accuracy, %) represents the proportion of pixels classified as cotton that are actually cotton, and $\boldsymbol{Recall}$ (i.e., Producer's Accuracy, %) represents the proportion of pixels that are actually cotton that are correctly classified. The value range of $\boldsymbol{F}1$-score is 0–1, and the closer the value is to 1, the better the classification effect is [33].

2.4.4. Cotton Yield Estimation Based on XGBoost

This study constructs an XGBoost regression model integrating multi-dimensional features to realize quantitative estimation of cotton yield in the Weigan River Basin [34]. The input features of the model include remote sensing time series indicators, meteorological driving factors, crop water stress index, and key radiation stress factors obtained from dust simulation (including PAR loss and aerosol optical depth). Hyperparameter optimization is performed using grid search combined with 5-fold cross-validation. The complete hyperparameter search space, optimal values, and model performance metrics are provided in Table S4. The coefficient of determination (R^2) and root mean square error (RMSE) are taken as core indicators to quantitatively evaluate the fitting effect and prediction accuracy of the model, so as to provide a reliable quantitative basis for evaluating the impact of radiation stress caused by dust on cotton yield. The definitions of the above evaluation indicators are as follows:

$$R^2 = 1 - \frac{\sum_i (\hat{y}_i - y_i)^2}{\sum_i (\overline{y}_i - y_i)^2} \tag{5}$$

$$\boldsymbol{RMSE} = \sqrt{\frac{1}{n}\sum_{i=1}^{n}(y_i - \hat{y}_i)^2} \tag{6}$$

where $\boldsymbol{n}$ is the total number of samples, y_i is the measured cotton yield of the i-th sample, $\hat{y}_i$ is the yield prediction value of the model, and $\overline{y}_i$ is the average value of the measured yield. The value range of R^2 is 0–1, and the closer the value is to 1, the better the model fitting effect is. The unit of ***RMSE*** is consistent with that of yield, and the smaller the value is, the higher the prediction accuracy is.

2.4.5. Impact Assessment and SHAP Interpretation

To quantitatively characterize the spatial response relationship between PAR loss and cotton yield, GPP at the pixel scale, this study adopts Pearson correlation analysis and linear regression analysis methods. All correlation tests were performed at a significance level of $\alpha = 0.05$. Given the large number of pixels involved and the risk of false positives in multiple testing, we focused on spatially continuous significant regions rather than isolated pixels, following common practices in remote sensing correlation analysis.

Meanwhile, the SHAP (SHapley Additive exPlanations) interpretability framework is introduced to deconstruct the XGBoost yield estimation model [35]. SHAP values were computed using the TreeExplainer adapted for ensemble tree models, which provides consistent and unbiased estimation for XGBoost. Partial dependence plots combined with SHAP summary plots were further used to identify the nonlinear response mode and critical stress threshold of radiation attenuation affecting yield, and also help to clarify the interaction mechanism between PAR loss and high temperature stress. The above analyses jointly and comprehensively explain the paths and modes of dust radiative forcing inhibiting cotton productivity. The calculation formula of the Pearson correlation coefficient (r) is as follows:

$$\boldsymbol{r} = \frac{\sum_{i=1}^{n}(\boldsymbol{x_i} - \overline{\boldsymbol{x}})(\boldsymbol{y_i} - \overline{\boldsymbol{y}})}{\sqrt{\sum_{i=1}^{n}(\boldsymbol{x_i} - \overline{\boldsymbol{x}})^2}\sqrt{\sum_{i=1}^{n}(\boldsymbol{y_i} - \overline{\boldsymbol{y}})^2}} \tag{7}$$

where $\boldsymbol{n}$ is the number of pixel samples, $\boldsymbol{x_i}$ is the PAR loss (ΔPAR) of the i-th pixel, $\overline{\boldsymbol{x}}$ is the average value of ΔPAR, $\boldsymbol{y_i}$ is the cotton yield or GPP of the i-th pixel, and $\overline{\boldsymbol{y}}$ is the average value of the corresponding variable. The value range of the correlation coefficient $\boldsymbol{r}$ is -1 to 1, a positive value indicates positive correlation, a negative value indicates negative correlation, and the larger the absolute value is, the stronger the correlation is.

3. Results

3.1. Spatial Distribution and Dynamic Changes in Cotton

This study first carries out cultivated land masking processing based on the GLC_FCS30D global 30 m land cover dataset [36]. The spatial pattern and area statistical results of each land cover type are shown in Figure S1 and Table 2. In the past 10 years, the study area has shown an obvious evolution trend of cultivated land expansion, construction land growth, and unused land reduction [37]. Unused land is still the dominant landscape type in the study area, and its area decreased significantly from 422.69 $\times$ 10^3 ha in 2012 to 410.26 $\times$ 10^3 ha in 2022, indicating that the intensity of land development is continuously improving. The cultivated land expansion is remarkable, with its area increasing from 98.51 $\times$ 10^3 ha to 108.60 $\times$ 10^3 ha, an increase of about 10%, which may be driven by land consolidation and agricultural reclamation policies. The area of construction land increased from 41.0 $\times$ 10^3 ha to 64.1 $\times$ 10^3 ha, with an obvious growth peak in 2019–2020. The areas of forest land and grassland are relatively stable, with only small fluctuations. The ice and snow coverage area shows an overall growth trend, increasing from 286.3 $\times$ 10^3 ha to 316.1 $\times$ 10^3 ha, which may be related to climate fluctuation. Water bodies and wetlands show a fluctuating downward trend, among which the water area decreased significantly after 2013 and then stabilized at a low level.

Table 2. Area changes in seven land use types in the Weigan River Basin from 2012 to 2022 (ha).

Year	Cropland	Forest Land	Grassland	Wetland	Built-Up Land	Unused Land	Water Body	Snow and Ice
2012	98,505	8463	69,209	2213	4101	422,685	5171	28,633
2013	99,841	9079	69,348	2664	4243	418,861	3727	31,218
2014	100,435	9069	69,509	2734	4342	417,935	3595	31,361
2015	101,377	8490	69,707	2419	4396	417,387	3682	31,521
2016	102,728	7624	70,399	2171	4341	416,649	3723	31,345
2017	103,997	7582	70,553	2233	4241	415,145	3751	31,479
2018	105,624	8167	69,855	2160	4318	413,348	3781	31,727
2019	106,179	8339	69,943	2418	4600	411,769	3925	31,806
2020	107,274	8244	69,320	2112	4577	411,327	3947	32,181
2021	108,126	8125	69,019	2254	4425	410,879	4095	32,058
2022	108,599	8109	69,867	2179	4271	410,259	4087	31,609

This study adopts the Random Forest algorithm to process Harmonized Landsat and Sentinel-2 (HLS) data and classifies four main types of crops in the study area, namely cotton, rice, wheat, and corn. The cross-validation method is used to evaluate the classification effect, and the accuracy indicators and confusion matrix are shown in Figure S2 and Figure S3, respectively [38]. The recognition accuracy of cotton is the highest, with a producer accuracy of 0.97, a classification accuracy rate of 91.8%, and the highest F1-score, which reflects that cotton has unique spectral and phenological characteristics. The classification performance of rice and corn is moderate: the user accuracy of rice is 0.87, and although corn has relatively high accuracy, its producer accuracy is only 0.66, indicating obvious omission errors. The classification accuracy of wheat is relatively low. The confusion matrix shows that most misclassification cases are marking other crops as cotton, 27.5% of wheat samples, and 27.3% of corn samples are misidentified, which is most probably caused by overlapping crop spectral characteristics or similar phenology during the key growth period. In general, the above results confirm the reliability of combining the Random Forest classifier with multi-temporal HLS data for crop mapping in heterogeneous agricultural landscapes.

Spatial analysis results show that the regional planting structure has significant agglomeration characteristics and a dynamic expansion trend (Figure 3). Cotton has always been the dominant crop in the region, occupying most of the oasis areas in the south and east of the study area. With the passage of time, as of 2022, the contiguous planting integration and expansion trend of its planting area is more prominent. Rice is mainly distributed in the north-central region, with a relatively stable spatial distribution pattern, and a small expansion was observed in 2022. Wheat and corn are mixedly distributed in marginal areas or specific irrigation areas. It is worth noting that wheat planting in the northwest has shown a concentration trend after 2017. Such spatiotemporal evolution characteristics reflect the transformation trend of regional agriculture gradually concentrating on dominant crops, indicating that land use efficiency has been improved.

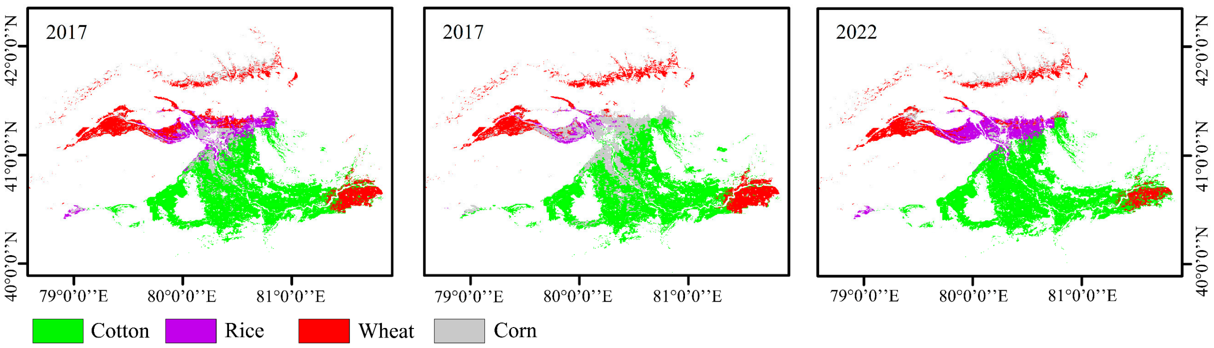

Figure 3. This figure shows the spatial distribution of four main crops (cotton, rice, wheat, and corn) in 2012, 2017, and 2022, and different crops are represented by distinct colors.

3.2. Simulation and Analysis of Temporal and Spatial Characteristics of Dust Aerosols

This study used monitoring data from March to September of 2012, 2017, and 2022 to analyze the temporal and spatial dynamic characteristics of aerosol optical depth in the study area (Figure 4). In the temporal dimension, aerosol concentration shows strong seasonality, peaking in spring, and then gradually declining in summer and autumn [39]. Dust activities intensify in March and peak annually in April, with mean concentrations exceeding 380 $\mu g \cdot m^{-3}$. Concentrations reached above 420 $\mu g \cdot m^{-3}$ in April 2012 and 2022, while the 2017 peak was approximately 395 $\mu g \cdot m^{-3}$, indicating strong interannual fluctuation. The concentration gradually decreases from May and drops to the lowest value of 150–200 $\mu g \cdot m^{-3}$ in July and August. The interannual fluctuation characteristics are obvious. For example, in June 2022, the concentration decline rate was slower, and the duration of the high concentration plateau period was longer. In the spatial dimension, the study area has strong heterogeneity, and the concentration shows the characteristics of high in the southeast and low in the northwest, and the highest value in the central and southeastern regions can reach 772.44 $\mu g \cdot m^{-3}$. The coverage of dust aerosols expands significantly from March to May, shrinks sharply after June, and has changed from a high-concentration red area to a large-scale low-concentration blue area by late summer.

To ensure the accuracy of WRF-Chem simulation results, this study uses the spatiotemporal dust data corresponding to the MERRA-2 (Modern-Era Retrospective analysis for Research and Applications, Version 2) reanalysis product to conduct regional-scale validation, and combines AERONET (Aerosol Robotic Network) site data to carry out point-scale validation, so as to comprehensively verify the applicability of the model in the study area. The validation time range covers the entire study period (March to September of 2012, 2017, and 2022), consistent with the time range of the remote sensing data and field observation data, ensuring the consistency and comprehensiveness of the validation. For spatial matching, since the spatial resolution of MERRA-2 is 0.5° $\times$ 0.625° and the WRF-Chem model is 1 km, the average value of simulated dust concentration of all WRF-Chem grid units within each MERRA-2 grid is extracted for comparison, and the spatial registration is completed by using the nearest neighbor interpolation method to ensure the rationality of spatial matching. A total of more than 600 groups of paired data points were used for linear regression analysis, and the results show that the WRF-Chem simulation results are in good agreement with the MERRA-2 data, with a coefficient of determination (R^2) of 0.62 (Figure S4). For point-scale validation, 3 AERONET sites distributed in the study area were selected, and the simulated dust concentration of WRF-Chem at the corresponding grid points was compared with the measured data of the sites. The results show that the root mean square error (RMSE) is 32.7 $\mu g \cdot m^{-3}$, and the mean absolute error (MAE) is 25.3 $\mu g \cdot m^{-3}$, indicating that the model has good simulation accuracy at both regional and point scales, which verifies the applicability of WRF-Chem in the study area. Note that MERRA-2 is a reanalysis product rather than in situ observation data, which introduces certain inherent uncertainties to the model validation results.

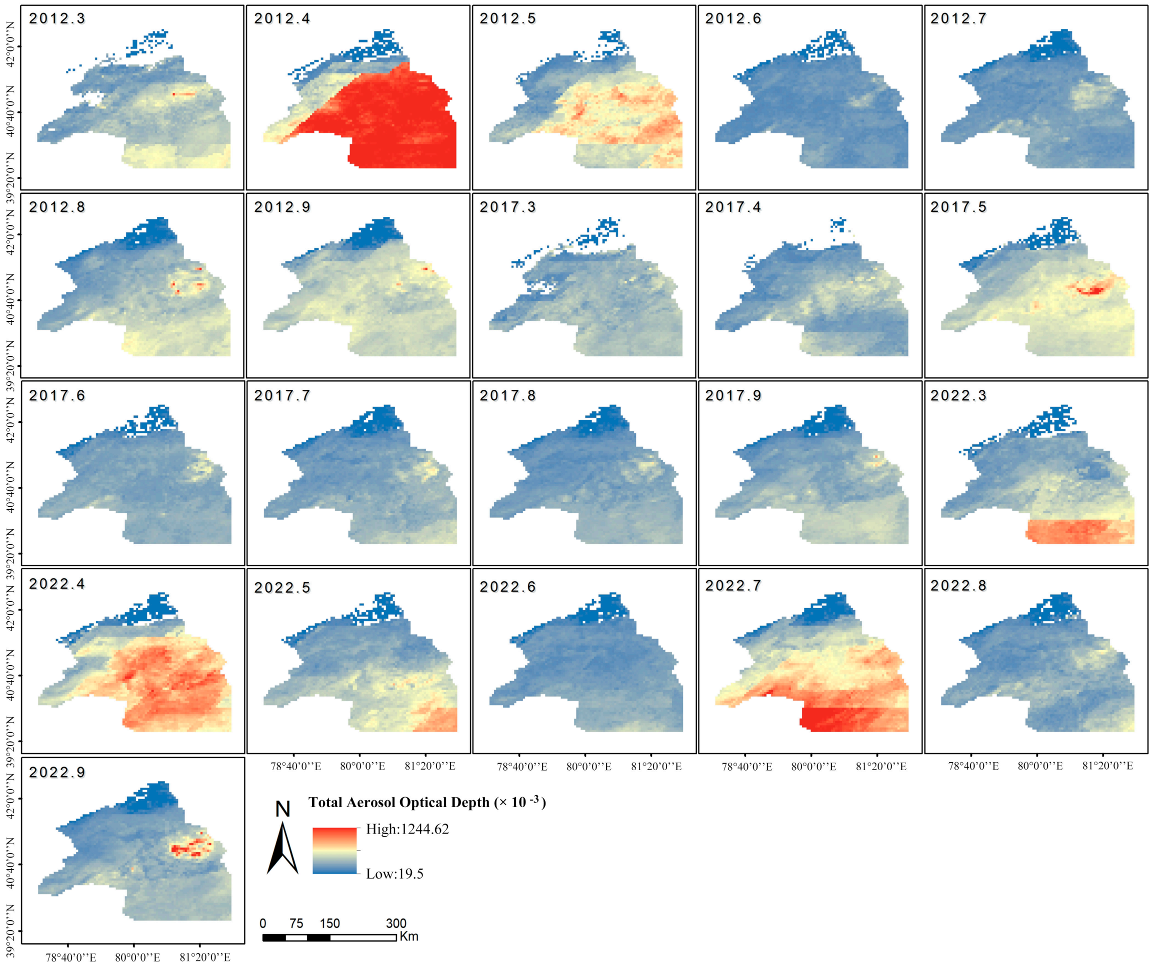

Figure 4. Grid map of the monthly spatial distribution of total aerosol concentration from 2012 to 2022. The color gradient (from blue to red) represents the concentration level. Each map contains a date, scale bar, and north arrow, which can clearly reflect the temporal and spatial distribution law.

As shown in Figures 5 and 6, the monthly average dust concentration simulated by WRF-Chem shows significant temporal and spatial heterogeneity. Spatially, high dust pollution is concentrated in the eastern and south-central parts of the study area, which is consistent with the distribution of desertified land around the Tarim Basin. In the spring of 2012, a large area of high concentration appeared. From 2017 to 2022, the main high-concentration core area shrank to some extent, but there were still persistent local hot spots. In March and June 2022, the dust concentration increased significantly, and the spatial distribution was more fragmented, indicating that local dust emission has increased [40].

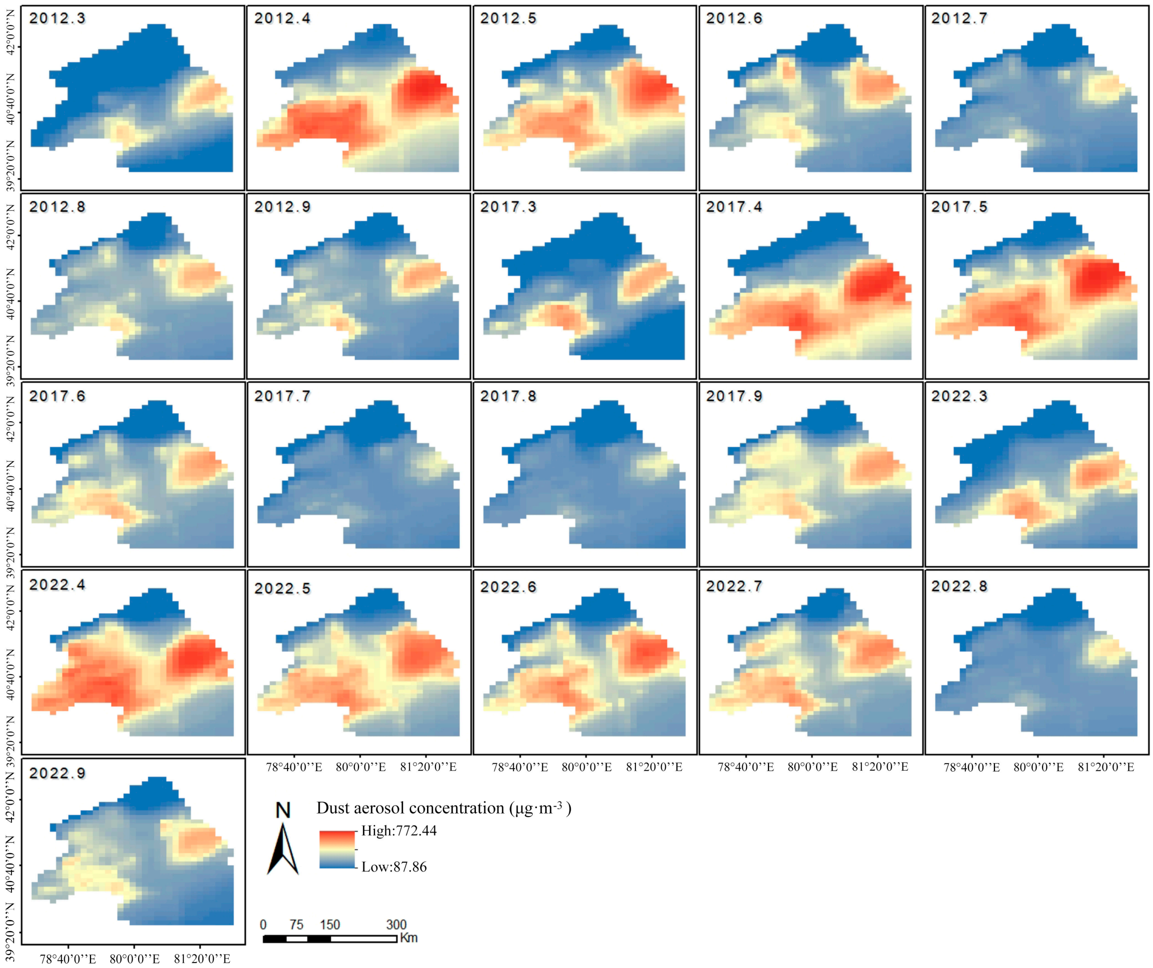

Figure 5. Temporal and spatial distribution map of dust aerosol concentration ($\mu g \cdot m^{-3}$) from March to September of 2012, 2017, and 2022. The concentration level is represented by a color gradient from blue to red, and is equipped with a legend, north arrow, and scale bar. The multi-year monthly sequence can clearly reflect the seasonal variation and interannual difference in dust load in the whole region.

3.3. Temporal and Spatial Pattern of Cotton GPP and Yield

This study analyzed the spatial pattern of monthly GPP in the study area in 2012, 2017, and 2022 (Figure S5). GPP has significant seasonal periodicity and obvious interannual variation, and high values are always concentrated in irrigated oases and near-water areas, confirming that water availability is the core limiting factor of arid ecosystem productivity [41]. Compared with 2012, the spatial connectivity of high GPP areas in 2017 and 2022 has improved, and the coverage in summer is wider, indicating that the vegetation carbon sequestration capacity has steadily improved. However, the overall level of GPP decreased in July 2022, indicating that short-term environmental stress had a significant impact.

The multi-source feature-driven cotton yield estimation model constructed by this study, based on the XGBoost machine learning framework, has robust accuracy, with a coefficient of determination (R^2) of 0.718 and a root mean square error (RMSE) of 457.5 $kg \cdot ha^{-1}$, which can realize reliable spatial mapping of yield in the study area. The simulated cotton yields of the Weigan River Basin in 2012, 2017, and 2022 show a stable spatial pattern of "high in the center and low at the edge" (Figure 7): high-yield areas are concentrated in irrigated oasis plains, and yields in desert edge areas are low due to soil salinization, water shortage, topography, and other factors. Cotton yield has shown a significant upward trend in the past ten years, which is manifested in the expansion of high-yield areas and the integration of fragmented plots [42]. This improvement benefits from the promotion of improved varieties, the application of precision agricultural technology, land remediation, the construction of high-standard farmland, and the popularization of drip irrigation technology, which have improved the resilience of the agricultural system under climate fluctuations.

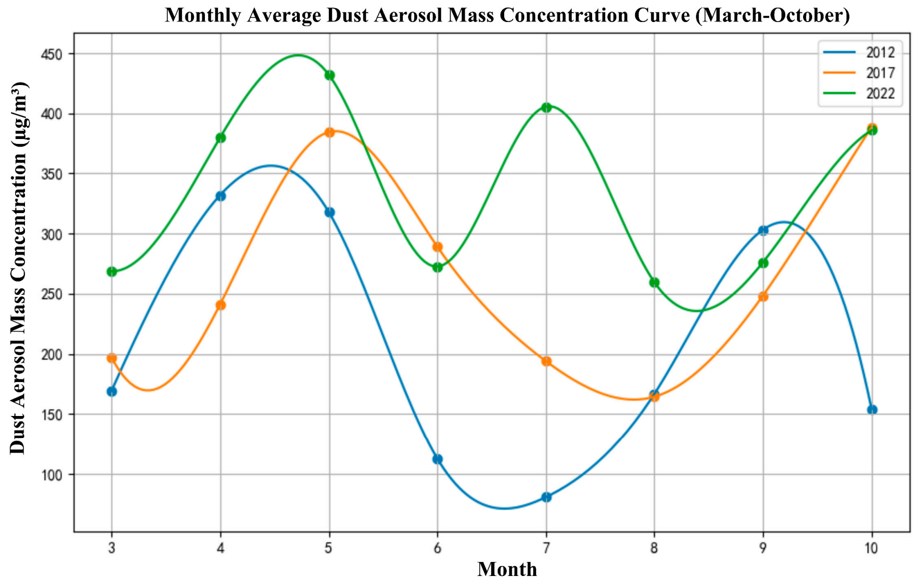

Figure 6. Monthly average change map of dust aerosol concentration from March to September of 2012, 2017, and 2022. This line chart compares the concentration change trends of the three years, and is equipped with a legend, coordinate axis labels, and a clear grid background for easy reading.

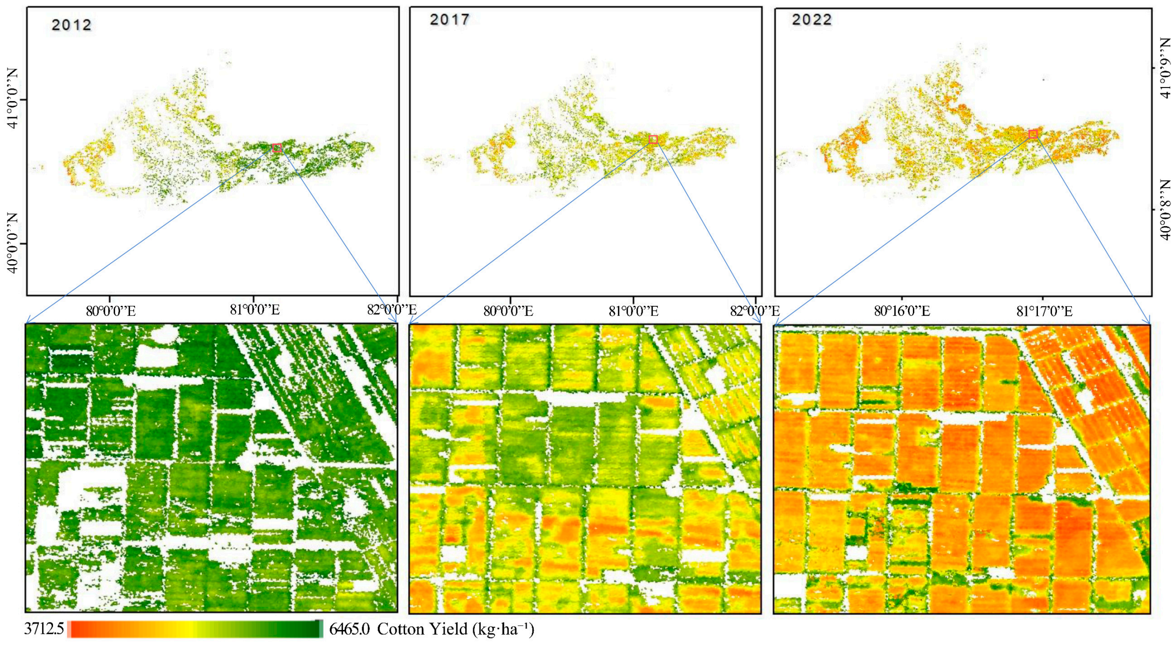

Figure 7. Distribution map of simulated cotton yield (kg·ha^{-1}) in 2012, 2017, and 2022, with spatial differences represented by a color gradient from 3712.5 kg·ha^{-1} to 6465.0 kg·ha^{-1}.

https://doi.org/10.3390/su18147443

3.4. Temporal and Spatial Distribution of Total Column Concentration of Aerosols

3.4.1. Temporal and Spatial Distribution Characteristics of PAR

LibRadtran simulation results show that dust has a significant attenuation effect on PAR and has a strong negative correlation with aerosol optical depth [15]. Figures S6 and Figure 8 show its temporal and spatial pattern: spatially, there is an obvious north–south gradient, the aerosol load in the northern region is low, and PAR is maintained above 180 W·m^{-2}; a PAR "shadow area" is formed in the dust plume area in the central and eastern parts, as low as about 160 W·m^{-2}, which is 15% lower than the clear sky potential value (>188 W·m^{-2}). As mentioned above, spring dust outbreaks lead to the maximum PAR attenuation, with the peak PAR loss rate of 55–57% occurring from March to May during cotton's critical growth stage (Figure S7). This attenuation effect originates from the absorption and forward scattering effects of coarse-grained dust, and the resulting radiation loss exceeds the gain brought by scattered light. In addition to radiation effects, dust may also change the surface energy balance and damage stomatal function, reflecting complex aerosol-radiation-ecological feedback. Severe PAR loss in spring greatly limits photosynthesis and gross primary productivity, which is the main way that dust restricts agricultural production in arid areas [17].

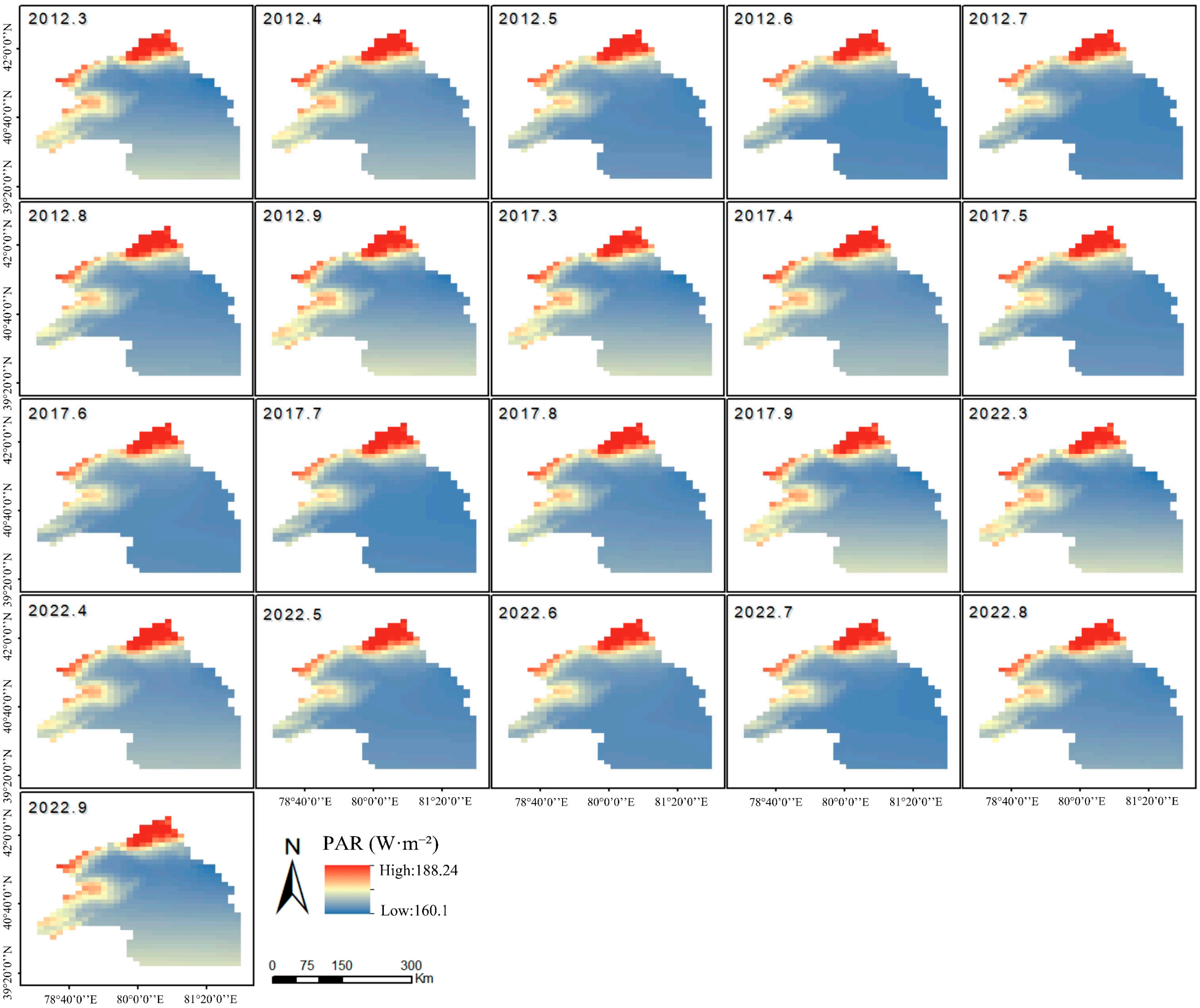

Figure 8. Spatial and temporal distribution of simulated PAR during the cotton growing season.

3.4.2. Impact of PAR Loss on Cotton GPP and Yield

The spatial correlation analysis between PAR loss caused by dust and cotton GPP shows a significant negative correlation in core agricultural areas ($r < -0.6$) [43]. Among the interannual yield variations in 2012, 2017, and 2022, 12–17% can be explained by PAR loss (Figure S8). The correlation coefficient (R) ranges from −0.37 to 0.71 (Figure 9): strong negative correlation corresponds to areas where the average daily PAR loss exceeds 20 $W \cdot m^{-2}$, and SHAP analysis identifies this value as the critical threshold, after which the yield shows a nonlinear downward trend with the increase in PAR loss. The most sensitive period of cotton to this radiation stress is the flowering and boll-forming period (July–August). On the contrary, the two are positively correlated in irrigated areas, because the dust peak period exactly corresponds to the period of high seasonal background radiation. It is worth noting that although the PAR loss was the highest in 2022 (75.8 $W \cdot m^{-2}$), the cotton yield was not the lowest, and the yield response curve was significantly flatter. Under the background of simultaneous extreme high temperature in 2022, the shading effect brought by dust may have a compensatory mitigation effect on heat stress; in addition, the good irrigation conditions in the study area and the strong stress resistance of cotton varieties also reduce the impact of PAR loss on yield, which explains why the yield does not show an extreme reduction even though the PAR loss far exceeds the critical threshold. Therefore, the net impact of dust on GPP is jointly determined by three factors: direct radiation attenuation, potential gain of scattered light, and interaction with extreme temperatures in the same period. As shown in Figures S9, Figures 10 and 11, this spatial heterogeneity is further verified, and significant negative correlations are detected in 87% of the cultivated land, which proves that radiation loss is a widespread limiting factor for regional cotton production.

In summary, the research results confirm that the direct radiative forcing of dust aerosols is the main, widely distributed way to inhibit yield, and its impact exceeds that of local management factors, highlighting a key environmental vulnerability in the reproductive growth stage of crops.

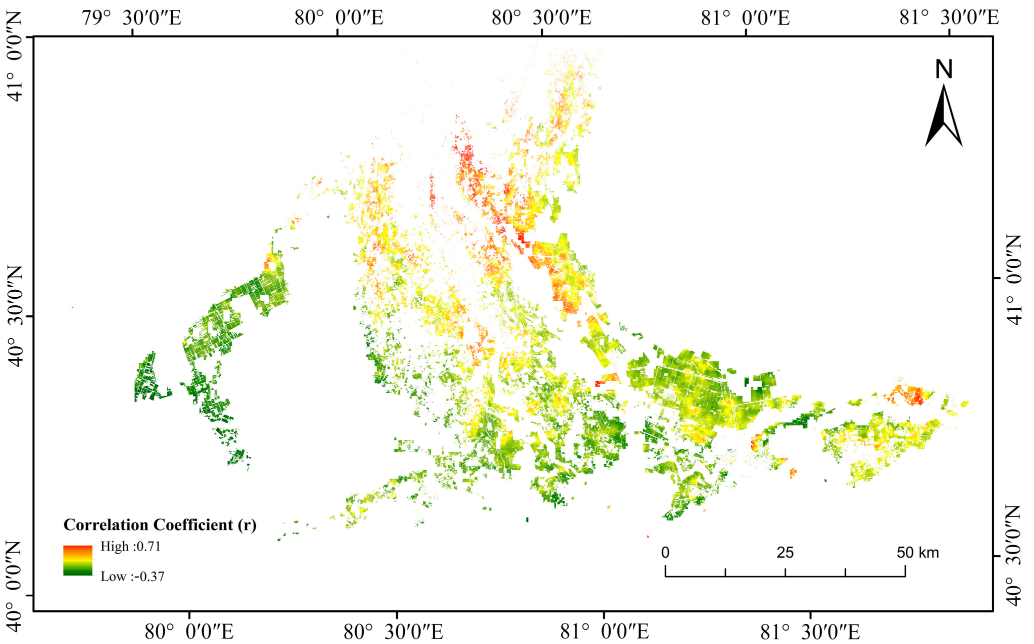

Figure 9. Spatial distribution of correlation coefficient (R) between cotton yield and dust-induced PAR loss in the Weigan River Basin. Color gradients from −0.37 (green) to 0.71 (red); map includes north arrow and scale bar (km).

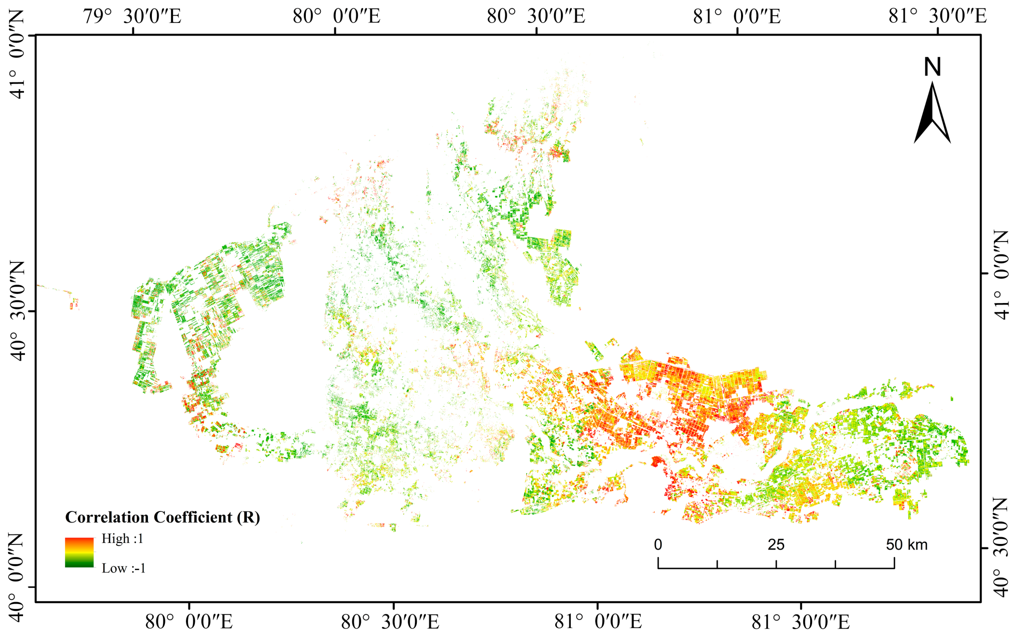

Figure 10. Spatial distribution of the correlation coefficient (R) between PAR loss and cotton yield.

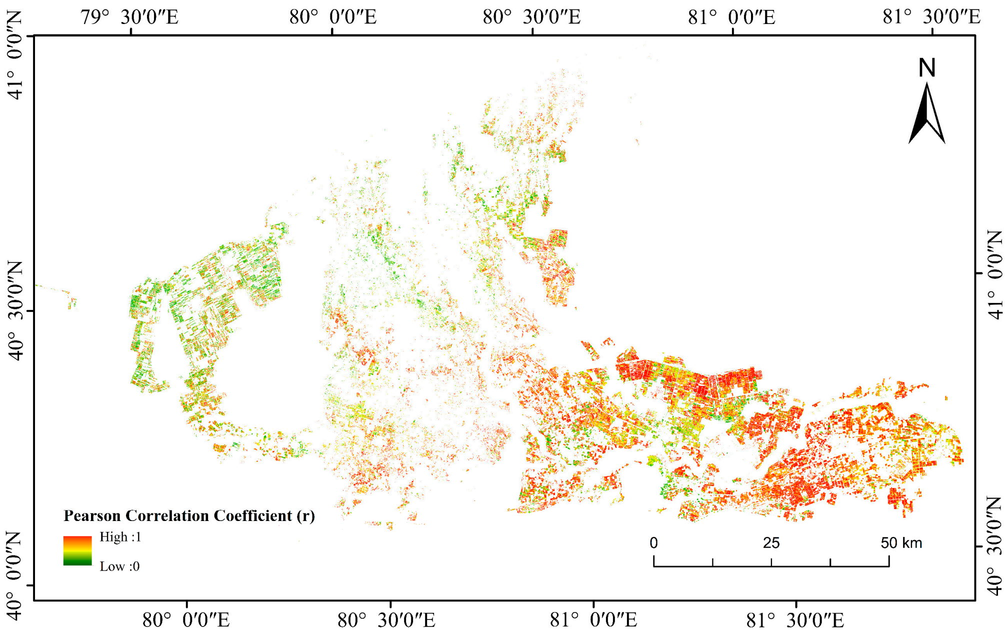

Figure 11. *p*-value distribution map of Pearson correlation between PAR loss and cotton yield.

4. Discussion

4.1. Mechanism of Dust Aerosol Affecting Cotton Physiology

Unlike previous studies that assumed a linear response, our SHAP analysis reveals a nonlinear threshold and first confirms that the main way that dust aerosols inhibit cotton productivity on a regional scale is direct radiative forcing. Spatial analysis shows that in up to 87% of cotton fields, PAR loss is statistically significantly negatively correlated with yield, which proves from a statistical point of view that radiation attenuation is a ubiquitous environmental stress factor, and its impact is not interfered with by differences in field management measures. Nationwide-scale research also verified the inhibitory effect of aerosol radiation attenuation on terrestrial photosynthesis [18].

More importantly, the research results show that this effect is not a simple linear relationship. SHAP analysis identifies a clear nonlinear threshold: when the average daily PAR loss exceeds 20 W·m^{-2}, cotton yield begins to decline at an accelerated rate. This threshold may have important physiological significance, and most likely corresponds to a critical point in the flowering and boll-forming period [44]. The flowering and boll-forming period is the peak stage of cotton light demand, which plays a decisive role in the formation of final yield. Therefore, the threshold of 20 W·m^{-2} may mark the critical point where the cotton photosynthetic system can no longer maintain the balance between photosynthetic output and the metabolic demand for boll development. When PAR loss is lower than this threshold, crops can partially compensate through internal physiological adjustment; but once it exceeds this value, photosynthetic products will drop sharply, directly hindering the normal development of cotton bolls, leading to increased boll shedding and reduced boll weight, and thus the yield loss shows a nonlinear intensification trend [45]. Therefore, 20 W·m^{-2} is not only a statistical inflection point but also can be regarded as an ecophysiological threshold with early warning significance.

4.2. Dual Effects: Radiation Attenuation vs. High Temperature Mitigation

A noteworthy phenomenon was observed in 2022: despite the PAR loss reaching as high as 75.8 W·m^{-2}, the sensitivity of yield to radiation loss (i.e., the regression slope) was gentler compared with other years. While the yield reduction (382.3 kg·ha^{-1}) fell short of the model RMSE (457.5 kg·ha^{-1}), the significant yield gap ($p < 0.05$) and the distinct nonlinear threshold identified by SHAP analysis confirm that dust-induced PAR decline drove the loss, rather than model uncertainty. This study holds that this reflects the positive regulatory effect of dust under simultaneous extreme high temperature conditions (especially when the daily maximum temperature exceeds 35 °C) [46]. This mechanism is essentially different from the diffuse light fertilization effect reported in forest ecosystems [47]. In oasis irrigated agricultural systems with sufficient water, the main limiting factor for crop growth has shifted from water availability to light and temperature conditions. The shading effect brought by dust can reduce canopy temperature and vapor pressure deficit under extreme high temperatures, thereby alleviating photoinhibition and stomatal limitation [48]. This regulatory effect can offset the photosynthetic potential loss caused by the reduction in total radiation to a certain extent [20].

The physiological mechanisms underlying this heat-alleviation effect are hypothesized to involve three interconnected pathways. First, under high temperature stress, cotton plants typically respond by increasing stomatal conductance to enhance transpirational cooling, yet this strategy comes at the cost of accelerated water loss and potential hydraulic dysfunction [49]. The shading effect of dust aerosols reduces incoming solar radiation and lowers canopy temperature, thereby decreasing the vapor pressure deficit (VPD) between the leaf and the atmosphere. This reduction in VPD may allow stomata to maintain adequate conductance for CO_2 uptake while reducing transpirational demand, potentially balancing the trade-off between cooling and water conservation [50]. Second, high temperatures exacerbate photoinhibition by impairing the repair of photosystem II (PSII) and increasing the production of reactive oxygen species (ROS) in the thylakoid membranes. The reduction in excess light energy under dust shading diminishes the excitation pressure on PSII, which may help alleviate photoinhibitory damage and preserve the photochemical efficiency of cotton leaves [51]. Third, the combination of reduced canopy temperature and moderated VPD may suppress the heat-induced acceleration of dark respiration and photorespiration, which are major carbon losses under high temperature conditions [50]. By mitigating these non-stomatal limitations to photosynthesis, dust shading may help sustain net carbon assimilation rates even when total incident radiation is reduced. Together, these physiological adjustments offer a plausible explanation for why cotton yield in 2022 did not exhibit the extreme reduction that would be expected from the 75.8 $W \cdot m^{-2}$ PAR loss alone, highlighting the importance of considering both stomatal and non-stomatal responses when evaluating aerosol impacts on crop productivity under compound heat–dust events.

An important inference can be drawn from this: against the background of climate change and frequent extreme high temperature events, the net effect of dust aerosols on agriculture in arid areas may become more complex and uncertain. Future assessment models must be able to couple the interaction effects of radiation and temperature (and vapor pressure deficit); otherwise, they may systematically overestimate the negative impact of dust in high-temperature years.

4.3. Spatial Heterogeneity and Yield-Level Dependence

The impact of dust aerosols on cotton productivity exhibits significant spatial heterogeneity and yield-level dependence. In high-yield areas (>5250 $kg \cdot ha^{-1}$, concentrated in well-irrigated oasis cores), the correlation coefficient between PAR loss and yield is $r < -0.6$, indicating that dust radiative forcing is the primary meteorological risk factor. In low-yield areas (<3900 $kg \cdot ha^{-1}$, distributed in desert-edge saline-alkali and water-deficient regions), water and fertilizer constraints dominate production limitations, and dust shading may even slightly alleviate heat stress, showing weak positive or neutral effects.

This "low-yield mitigation, high-yield aggravation" asymmetric characteristic essentially reflects the difference in limiting factor hierarchy at different yield levels. In low-yield stages, light, water, and fertilizer are all hard constraints, and the negative effect of dust light attenuation is masked by other stresses. In high-yield stages, water and fertilizer are saturated, and light becomes the only bottleneck, making dust radiative forcing the decisive factor. This spatial differentiation mechanism provides a scientific basis for differentiated management strategies: high-yield fields should focus on dust monitoring and early warning, while low-yield fields should prioritize irrigation and soil improvement.

4.4. Phenological Sensitivity and Critical Window

The flowering-to-boll-forming period (July–August) is identified as the critical window in which PAR loss exceeding 20 $W \cdot m^{-2}$ triggers nonlinear yield decline. During this stage, cotton boll development has the highest demand for photosynthetic products, and the balance between photosynthetic supply and metabolic demand directly determines final yield. SHAP analysis confirms that the negative response of yield intensifies nonlinearly when PAR loss exceeds the threshold; frequent dust events during this phenological stage inhibit gross primary productivity, leading to reduced boll weight and increased boll shedding rate.

Notably, dust events are concentrated in April–June (spring), overlapping with the seedling and squaring stages, while the flowering-to-boll stage (July–August) has relatively lower dust intensity. However, the flowering-to-boll stage is the most sensitive period because: (1) the cotton canopy is not yet fully closed, with weak light interception capacity, making it highly sensitive to radiation fluctuations; (2) this stage is the core window for photosynthetic product transfer to bolls, and boll weight and seed cotton formation rate directly depend on current photosynthetic supply; (3) strong dust processes during this stage, though less frequent, are more likely to cause boll shedding due to the high metabolic demand. This phenological sensitivity provides a precise time target for field management: the 20-day window around the flowering-to-boll stage is the key period for dust impact prevention and control.

4.5. The "Technology-Environment Dual Margin" Constraint Framework

Based on the ten-year sequential monitoring results, this study further refines the "technology-environment dual margin" constraint framework for oasis agriculture in arid regions. The productivity ceiling of irrigated cotton areas is always constrained by two conditions: the human regulation margin determined by agricultural technology upgrading, and the natural environmental margin determined by regional ecological carrying capacity. At different production stages, the dominance of these two constraints differs significantly. If the technology improvement space is exhausted first while environmental conditions remain relatively stable, yield will maintain high-level stability relying on favorable growth environments. If environmental stress reaches critical intensity first, even when field management and variety technology are mature, productivity will enter a stable stage prematurely, forming a pseudo-technology bottleneck that appears to be technology stagnation but is actually an environmental limitation. The productivity plateau in the Weigan River Basin after 2016 is a typical case where the environmental margin was triggered first: the continuous photosynthetic loss caused by dust radiative attenuation became the core factor that first constrained productivity breakthrough. This mechanism also reasonably explains the current production contradiction: although regional ecological sand control projects have effectively reduced overall dust load, cotton productivity remains difficult to break through the bottleneck. Single ecological improvement can only weaken environmental stress intensity, but cannot completely remove the limiting factor of radiation conditions on photosynthetic production. Therefore, to achieve stable yield increase and break existing productivity limitations in arid cotton areas, it is not sufficient to rely solely on traditional agricultural technology upgrading. It is also necessary to carry out targeted field management matching regional dust stress characteristics: selecting stress-resistant varieties, optimizing cultivation models to consolidate production foundations, while relying on dust monitoring and early warning, and key growth stage protection and regulation to weaken environmental stress, breaking through productivity bottlenecks through synergistic improvement of technology optimization and environmental adaptation.

4.6. Limitations and Uncertainties

The core contribution of the framework coupling WRF-Chem, LibRadtran, multi-source remote sensing, and machine learning constructed in this study lies in the realization of seamless integration of physical mechanism methods and data-driven methods in the spatial dimension: WRF-Chem and LibRadtran construct a physically consistent dust-radiation transmission chain, while high-resolution remote sensing observations and machine learning methods accurately capture the spatial heterogeneity of vegetation responses to radiation changes. This framework effectively solves the dual limitations that traditional ground observations are difficult to extrapolate, spatially pure statistical models lack physical interpretability, and cannot separate multiple stress interference. Most existing data-driven neural network frameworks only pursue fitting accuracy without embedding physical process constraints, limiting their ability to distinguish interactive environmental stressors [52].

(1) Uncertainty propagation: The WRF-Chem model contains inherent uncertainties associated with dust emission parameterization and soil moisture representation, which directly influence PAR loss simulation accuracy. Validation against MERRA-2 reanalysis data showed an R^2 of 0.62, RMSE of 32.7 $\mu g \cdot m^{-3}$, and MAE of 25.3 $\mu g \cdot m^{-3}$, indicating moderate but acceptable simulation uncertainty [53].

(2) Indirect characterization of crop physiology: In the existing framework, the correlation from radiation to photosynthesis and yield is still highly dependent on remote sensing proxy variables and statistical relationships, and most of the direct physiological

mechanisms are still indirectly characterized. In the future, Solar-Induced Chlorophyll Fluorescence (SIF) data can be integrated to realize direct remote sensing monitoring of photosynthesis, so as to clarify the physiological response mechanism of crops and provide a more direct means for verifying and quantifying the physiological effects of radiation stress [54].

(3) Lack of key feedback processes: This study only focuses on the direct radiation effect of dust aerosols, while dust deposition can provide essential mineral nutrients such as iron and phosphorus for the soil, which may have a long-term positive effect on barren soil; in addition, aerosols, as cloud condensation nuclei, can produce indirect effects, further changing regional precipitation and radiation budget [55]. Future integrated models need to incorporate these longer-term and more complex feedback loops.

4.7. Agronomic Strategies and Climate-Resilient Management Under Compound Heat–Dust Hazards

Combined with the revealed response mechanisms and critical stress threshold, we propose targeted regulation strategies to mitigate dust radiative stress and stabilize cotton yield in arid regions. For areas with severe dust influence and high cotton yield, dust monitoring and early warning systems should be established, focusing on the flowering-to-boll sensitive stage. Timely field water and foliage management can reduce yield loss caused by PAR attenuation. For marginal fields at the desert-oasis ecotone, priority should be given to improving irrigation and soil conditions. Meanwhile, selecting new cotton varieties with combined tolerance to low light and high temperature can enhance the comprehensive stress resistance of crops. The dual effect of dust should also be fully considered in regional agricultural planning: reasonable utilization of dust shading to relieve high-temperature damage while avoiding continuous radiation restriction. The above countermeasures can effectively reduce the risk of yield reduction under frequent dust events and promote the sustainable development of the cotton industry in arid areas. Beyond these general recommendations, our findings carry specific implications for the increasingly common compound heat–dust disaster scenarios in southern Xinjiang. As concurrent heatwaves and sandstorms become more frequent in the region [13], the dual biophysical effects of dust identified in this study—radiation attenuation suppressing photosynthesis while shading partially alleviates heat stress—offer unique decision-making references for climate-resilient oasis agriculture. Differentiated field regulation based on the 20 $W \cdot m^{-2}$ PAR loss threshold can balance the trade-off between light limitation and heat relief during cotton's flowering and boll-forming sensitive window. For high-yield core cotton fields, early dust warning and shading mitigation measures should be deployed when PAR loss approaches the critical value; for desert fringe low-yield plots, optimized irrigation can simultaneously alleviate heat and light dual stress under compound disaster conditions. The quantitative response relationship established in this paper fills the gap of targeted agronomic strategies under overlapping dust-heat stress scenarios.

5. Conclusions

This study develops an integrated framework that couples WRF-Chem atmospheric simulation, LibRadtran radiative transfer, multi-source remote sensing, and SHAP-based machine learning. The framework bridges regional aerosol processes and field-scale crop responses, a challenge previously unresolved in data-scarce arid regions. The SHAP module offers a transferable approach to isolate nonlinear radiative forcing signals from confounding covariates. Three core research findings are summarized as follows:

(1) Dust-induced PAR reduction imposes a nonlinear yield response with a critical threshold of 20 $W \cdot m^{-2}$. Below this value, cotton shows physiological compensation; above it, irreversible yield loss accelerates.

(2) The July–August flowering-to-boll stage is the most phenologically sensitive window, despite lower dust loading than spring, underscoring the importance of growth-stage susceptibility.
(3) Dust exerts dual biophysical regulation: radiation attenuation suppresses carbon assimilation, while shading partially offsets extreme heat damage, explaining the muted yield suppression under concurrent heat–dust events.

For practical application, the quantified threshold and sensitive window provide standardized benchmarks for regional dust early-warning systems tailored to oasis cotton. Differentiated management strategies are proposed: high-yield core zones require radiation stress mitigation during the sensitive reproductive stage, whereas desert-fringe plots benefit from optimized irrigation to relieve combined light and heat stress. These localized schemes support climate-resilient cotton cultivation under increasing compound heatwave–sandstorm disasters in southern Xinjiang.

Supplementary Materials: The following supporting information can be downloaded at: https://www.mdpi.com/article/10.3390/su18147443/s1, Table S1. Summary of data sources and specifications used in this study; Table S2. WRF-Chem model configuration; Table S3. LibRadtran configuration; Table S4. XGBoost hyperparameters and performance; Figure S1. Annual land-use spatial distribution maps illustrating land cover dynamic changes from 2012 to 2022; Figure S2. Crop classification confusion matrix and multi-index accuracy statistics of main crops; Figure S3. Quantitative comparison of Precision, Recall, and F1-score for cotton, rice, wheat, and maize classification; Figure S4. Validation scatter plot of simulated dust concentration from WRF-Chem against MERRA-2 reanalysis data; Figure S5. Monthly spatial distribution of GPP from March to September across 2012, 2017, and 2022; Figure S6. Spatiotemporal distribution of growing-season photosynthetically active radiation (PAR); Figure S7. Monthly dust-induced PAR reduction rate from March to September in 2012, 2017, and 2022; Figure S8. Linear correlation between dust-caused PAR loss and regional cotton GPP; Figure S9. Response relationship between dust-induced PAR attenuation and final cotton yield.

Author Contributions: Conceptualization, N.E., H.W., K.L. and X.A.; methodology, K.L., N.E., X.A., H.W., A.M., X.W. and Y.L.; software, K.L. and Y.L.; validation, K.L., X.A. and A.M.; formal analysis, K.L.; investigation, K.L., X.W., Y.L., N.E. and A.M.; resources, N.E., H.W. and X.A.; data curation, X.A., X.W. and A.M.; writing—original draft, K.L.; writing—review and editing, N.E., H.W., K.L., X.A., A.M. and X.W.; visualization, K.L., Y.L., X.W. and A.M.; supervision, N.E., H.W. and X.A. All authors have read and agreed to the published version of the manuscript.

Funding: This research was funded by the special fund of Xinjiang Key Laboratory of Soil and Plant Ecological Processes, grant number 24XJTRZW02, and the Autonomous Region Key Research and Development Project, grant number 2024B03023-2.

Institutional Review Board Statement: Not applicable.

Informed Consent Statement: Not applicable.

Data Availability Statement: The data presented in this study are available on request from the corresponding author. Due to the unfinished research project of our group, the measured experimental data cannot be publicly disclosed temporarily. Academic cooperation and data access can be communicated via email.

Acknowledgments: The authors appreciate the meteorological and field dataset support provided by the relevant agricultural and meteorological departments in Xinjiang during the research.

Conflicts of Interest: The authors declare no conflicts of interest. The funders had no role in the design of the study; in the collection, analyses, or interpretation of data; in the writing of the manuscript; or in the decision to publish the results.

Abbreviations

The following abbreviations are used in this manuscript:

AOD	Aerosol Optical Depth
AERONET	Aerosol Robotic Network
ECMWF	European Centre for Medium-Range Weather Forecasts
EVI	Enhanced Vegetation Index
ERA5-Land	ERA5 Land Reanalysis Dataset
GLC_FCS30D	Global Land Cover Fine Classification 30 m Dataset
GPP	Gross Primary Productivity
HLS	Harmonized Landsat and Sentinel
LST	Land Surface Temperature
LibRadtran	Library for Radiative Transfer
MERRA-2	Modern-Era Retrospective analysis for Research and Applications, Version 2
MODIS	Moderate Resolution Imaging Spectroradiometer
NDVI	Normalized Difference Vegetation Index
NDWI	Normalized Difference Water Index
NDRE	Normalized Difference Red Edge
PAR	Photosynthetically Active Radiation
RF	Random Forest
RMSE	Root Mean Square Error
SAR	Synthetic Aperture Radar
SHAP	SHapley Additive exPlanations
USGS	United States Geological Survey
WRF-Chem	Weather Research and Forecasting model coupled with Chemistry
XGBoost	Extreme Gradient Boosting

References

1. Vitale, G.S.; Scavo, A.; Zingale, S.; Tuttolomondo, T.; Santonoceto, C.; Pandino, G.; Lombardo, S.; Anastasi, U.; Guar Naccia, P. Agronomic Strategies for Sustainable Cotton Production: A Systematic Literature Review. *Agriculture* **2024**, *14*, 1597. [CrossRef]
2. Thevs, N.; Peng, H.; Rozi, A.; Zerbe, S.; Abdusalih, N. Water Allocation and Water Consumption of Irrigated Agriculture and Natural Vegetation in the Aksu-Tarim River Basin, Xinjiang, China. *J. Arid. Environ.* **2015**, *112*, 87–97. [CrossRef]
3. Wang, Y.; Peng, S.; Huang, J.; Zhang, Y.; Feng, L.; Zhao, W.; Qi, H.; Zhou, G.; Deng, N. Prospects for Cotton Self-Sufficiency in China by Closing Yield Gaps. *Eur. J. Agron.* **2022**, *133*, 126437. [CrossRef]
4. Xing, Y.; Chen, Y.; Yan, S.; Cao, X.; Zhou, Y.; Zhang, X.; Shi, T.; Niu, X.; Wu, D.; Cui, J.; et al. Dust Storms from the Taklamakan Desert Significantly Darken Snow Surface on Surrounding Mountains. *Atmos. Chem. Phys.* **2024**, *24*, 5199–5219. [CrossRef]
5. Yang, P.; Zhang, S.; Xia, J.; Chen, Y.; Zhang, Y.; Cai, W.; Wang, W.; Wang, H.; Luo, X.; Chen, X. Risk Assessment of Water Resource Shortages in the Aksu River Basin of Northwest China under Climate Change. *J. Environ. Manag.* **2022**, *305*, 114394. [CrossRef] [PubMed]
6. Abuduwaili, J.; Zhaoyong, Z.; Feng Qing, J.; Dong Wei, L. The Disastrous Effects of Salt Dust Deposition on Cotton Leaf Photo synthesis and the Cell Physiological Properties in the Ebinur Basin in Northwest China. *PLoS ONE* **2015**, *10*, e0124546. [CrossRef] [PubMed]
7. Tian, L.; Chen, L.; Zhang, P.; Bi, L. Estimating Radiative Forcing Efficiency of Dust Aerosol Based on Direct Satellite Observations: Case Studies over the Sahara and Taklimakan Desert. *Atmos. Chem. Phys.* **2021**, *21*, 11669–11687. [CrossRef]
8. Javad Ahmadi-Lahijani, M.; Moori, S. Photosynthetic Response and Adaptation of Plants in Perspective of Global Climate Change. In *Abiotic Stress in Plants—Adaptations to Climate Change*; Oliveira, M., Fernandes-Silva, A., Eds.; IntechOpen: Rijeka, Croatia, 2023; ISBN 978-1-83768-496-0.
9. Li, F.; Yigitcanlar, T.; Nepal, M.; Nguyen, K.; Dur, F. Machine Learning and Remote Sensing Integration for Leveraging Urban Sustainability: A Review and Framework. *Sustain. Cities Soc.* **2023**, *96*, 104653. [CrossRef]
10. Song, X.-P.; Huang, W.; Hansen, M.C.; Potapov, P. An Evaluation of Landsat, Sentinel-2, Sentinel-1 and MODIS Data for Crop Type Mapping. *Sci. Remote Sens.* **2021**, *3*, 100018. [CrossRef]
11. Yuan, T.; Chen, S.; Huang, J.; Zhang, X.; Luo, Y.; Ma, X.; Zhang, G. Sensitivity of Simulating a Dust Storm over Central Asia to Different Dust Schemes Using the WRF-Chem Model. *Atmos. Environ.* **2019**, *207*, 16–29. [CrossRef]

12. Meng, L.; Yang, X.; Zhao, T.; He, Q.; Mamtimin, A.; Wang, M.; Huo, W.; Yang, F.; Zhou, C.; Pan, H. Simulated Regional Transport Structures and Budgets of Dust Aerosols during a Typical Springtime Dust Storm in the Tarim Basin, Northwest China. *Atmos. Res.* **2020**, *238*, 104892. [CrossRef]
13. Liu, Y.; Huang, J.; Tan, Z.; Zhou, C.; Li, D.; Xie, Y. Compound Events of Heatwave and Dust Storm in the Taklamakan Desert. *Sci. China Earth Sci.* **2024**, *67*, 2073–2083. [CrossRef]
14. Ukhov, A.; Ahmadov, R.; Grell, G.; Stenchikov, G. Improving Dust Simulations in WRF-Chem v4.1.3 Coupled with the GOCART Aerosol Module. *Geosci. Model Dev.* **2021**, *14*, 473–493. [CrossRef]
15. Shi, K.; Zhang, Y.; Liu, X.; Wang, M.; Qin, B. Remote Sensing of Diffuse Attenuation Coefficient of Photosynthetically Active Radiation in Lake Taihu Using MERIS Data. *Remote Sens. Environ.* **2014**, *140*, 365–377. [CrossRef]
16. Shaamala, A.; Yigitcanlar, T.; Nili, A.; Nyandega, D. Machine Learning Applications for Urban Geospatial Analysis: A Review of Urban and Environmental Studies. *Cities* **2025**, *165*, 106139. [CrossRef]
17. Song, J.; Xia, X.; Che, H.; Wang, J.; Zhang, X.; Li, X. Daytime Variation of Aerosol Optical Depth in North China and Its Impact on Aerosol Direct Radiative Effects. *Atmos. Environ.* **2018**, *182*, 31–40. [CrossRef]
18. Jang, E.; Choi, S.; Yoo, E.; Hyun, S.; An, J. Impact of Shipping Emissions Regulation on Urban Aerosol Composition Changes Revealed by Receptor and Numerical Modelling. *npj Clim. Atmos. Sci.* **2023**, *6*, 52. [CrossRef] [PubMed]
19. Lesk, C.; Anderson, W.; Rigden, A.; Coast, O.; Jägermeyr, J.; McDermid, S.; Davis, K.F.; Konar, M. Compound Heat and Moisture Extreme Impacts on Global Crop Yields under Climate Change. *Nat. Rev. Earth Environ.* **2022**, *3*, 872–889. [CrossRef]
20. Schiferl, L.D.; Heald, C.L. Particulate Matter Air Pollution May Offset Ozone Damage to Global Crop Production. *Atmos. Chem. Phys.* **2018**, *18*, 5953–5966. [CrossRef]
21. Guo, S.; Liu, Y.; Sun, Y.; Zhou, H.; Gao, Y.; Wang, P.; Zhi, H.; Zhang, Y.; Gan, J.; Ning, S. Metabolic-Related Gene Prognostic Index for Predicting Prognosis, Immunotherapy Response, and Candidate Drugs in Ovarian Cancer. *J. Chem. Inf. Model.* **2024**, *64*, 1066–1080. [CrossRef] [PubMed]
22. Chen, J.; Shao, Z.; Zhu, H.; Chen, Y.; Li, Y.; Zeng, Z.; Yang, Y.; Wu, J.; Hu, B. Sustainable Interior Design: A New Approach to Intelligent Design and Automated Manufacturing Based on Grasshopper. *Comput. Ind. Eng.* **2023**, *183*, 109509. [CrossRef]
23. Bao, T.; Xi, G.; Deng, B.; Chang, I.-S.; Wu, J.; Jin, E. Long-Term Variations in Spatiotemporal Clustering Characteristics of Dust Events in Potential Dust Sources in East Asia. *CATENA* **2023**, *232*, 107397. [CrossRef]
24. Claverie, M.; Ju, J.; Masek, J.G.; Dungan, J.L.; Vermote, E.F.; Roger, J.-C.; Skakun, S.V.; Justice, C. The Harmonized Landsat and Sentinel-2 Surface Reflectance Data Set. *Remote Sens. Environ.* **2018**, *219*, 145–161. [CrossRef]
25. Wu, X.; Zou, B.; Lu, C.; Wang, L.; Zhang, Y.; Wang, H. Dynamic Security Computing Framework with Zero Trust Based on Privacy Domain Prevention and Control Theory. *IEEE J. Sel. Areas Commun.* **2025**, *43*, 2266–2278. [CrossRef]
26. Gao, B. NDWI—A Normalized Difference Water Index for Remote Sensing of Vegetation Liquid Water from Space. *Remote Sens. Environ.* **1996**, *58*, 257–266. [CrossRef]
27. Main-Knorn, M.; Pflug, B.; Debaecker, V.; Louis, J. Calibration and Validation Plan for the L2A Processor and Products of the Sentinel-2 Mission. *Int. Arch. Photogramm. Remote Sens. Spat. Inf. Sci.* **2015**, *XL-7*, 1249–1255. [CrossRef]
28. Qiao, Y.; Ji, D.; Shang, H.; Xu, J.; Xu, R.; Shi, C. The Fusion of ERA5 and MERRA-2 Atmospheric Temperature Profiles with Enhanced Spatial Resolution and Accuracy. *Remote Sens.* **2023**, *15*, 3592. [CrossRef]
29. Grell, G.A.; Peckham, S.E.; Schmitz, R.; McKeen, S.A.; Frost, G.; Skamarock, W.C.; Eder, B. Fully Coupled "Online" Chemistry within the WRF Model. *Atmos. Environ.* **2005**, *39*, 6957–6975. [CrossRef]
30. Liu, L.; Huang, X.; Ding, A.; Fu, C. Dust-Induced Radiative Feedbacks in North China: A Dust Storm Episode Modeling Study Using WRF-Chem. *Atmos. Environ.* **2016**, *129*, 43–54. [CrossRef]
31. Saidou Chaibou, A.A.; Ma, X.; Sha, T. Dust Radiative Forcing and Its Impact on Surface Energy Budget over West Africa. *Sci. Rep.* **2020**, *10*, 12236. [CrossRef] [PubMed]
32. Halder, K.; Srivastava, A.K.; Zheng, W.; Alsafadi, K.; Zhao, G.; Maerker, M.; Singh, M.; Guoging, L.; Ghosh, A.; Vianna, M.; et al. A Robust and Scalable Crop Mapping Framework Using Advanced Machine Learning and Optical and SAR Imageries. *Smart Agric. Technol.* **2025**, *12*, 101354. [CrossRef]
33. Faqe Ibrahim, G.R.; Rasul, A.; Abdullah, H. Improving Crop Classification Accuracy with Integrated Sentinel-1 and Sentinel-2 Data: A Case Study of Barley and Wheat. *J. Geovis. Spat. Anal.* **2023**, *7*, 22. [CrossRef]
34. Srinivas, P.; Suresh, A. An Efficient Cotton Yield Prediction Framework Using Remote Sensing Images. *Sens. Imaging* **2025**, *26*, 127. [CrossRef]
35. Xun, L.; Zhang, J.; Yao, F.; Cao, D. Improved Identification of Cotton Cultivated Areas by Applying Instance-Based Transfer Learning on the Time Series of MODIS NDVI. *CATENA* **2022**, *213*, 106130. [CrossRef]
36. Zhou, Y.; Li, Y.; Li, W.; Li, F.; Xin, Q. Ecological Responses to Climate Change and Human Activities in the Arid and Semi-Arid Regions of Xinjiang in China. *Remote Sens.* **2022**, *14*, 3911. [CrossRef]
37. Liu, Y.; Xue, J.; Gui, D.; Lei, J.; Sun, H.; Lv, G.; Zhang, Z. Agricultural Oasis Expansion and Its Impact on Oasis Landscape Patterns in the Southern Margin of Tarim Basin, Northwest China. *Sustainability* **2018**, *10*, 1957. [CrossRef]

38. Jamil, M.D.; Abbas, M.Z.; Saeed, M.F.; Jamal, A.; Mubeen, M.; Zakir, A.; Ahmad, I.; Jameel, R.; Pentoś, K.; Dewir, Y.H.; et al. Improved Early-Stage Crop Classification Using a Novel Fusion-Based Machine Learning Approach with Sentinel-2A and Landsat 8–9 Data. *Environ. Monit. Assess.* **2025**, *197*, 982. [CrossRef] [PubMed]
39. Newman, S.J.; Furbank, R.T. Explainable Machine Learning Models of Major Crop Traits from Satellite-Monitored Continent-Wide Field Trial Data. *Nat. Plants* **2021**, *7*, 1354–1363. [CrossRef] [PubMed]
40. Kim, K.; Kim, S.; Choi, M.; Kim, M.; Kim, J.; Shin, I.; Kim, J.; Chung, C.; Yeo, H.; Kim, S.; et al. Modeling Asian Dust Storms Using WRF-chem during the DRAGON-asia Field Campaign in April 2012. *JGR Atmos.* **2021**, *126*, e2021JD034793. [CrossRef]
41. Peng, H.; Jia, Y.; Zhan, C.; Xu, W. Topographic Controls on Ecosystem Evapotranspiration and Net Primary Productivity under Climate Warming in the Taihang Mountains, China. *J. Hydrol.* **2020**, *581*, 124394. [CrossRef]
42. Zhou, Y.; Li, F.; Xin, Q.; Li, Y.; Lin, Z. Historical Variability of Cotton Yield and Response to Climate and Agronomic Management in Xinjiang, China. *Sci. Total Environ.* **2024**, *912*, 169327. [CrossRef] [PubMed]
43. Xue, W.; Zhang, J.; Ji, D.; Che, Y.; Lu, T.; Deng, X.; Li, X.; Tian, Y.; Wei, J. Aerosol-Induced Direct Radiative Forcing Effects on Terrestrial Ecosystem Carbon Fluxes over China. *Environ. Res.* **2021**, *200*, 111464. [CrossRef] [PubMed]
44. Grundy, P.R.; Yeates, S.J.; Bell, K.L. Cotton Production during the Tropical Monsoon Season. I—The Influence of Variable Radiation on Boll Loss, Compensation and Yield. *Field Crops Res.* **2020**, *254*, 107790. [CrossRef]
45. Yang, H.; Dong, B.; Wang, Y.; Qiao, Y.; Shi, C.; Jin, L.; Liu, M. Photosynthetic Base of Reduced Grain Yield by Shading Stress during the Early Reproductive Stage of Two Wheat Cultivars. *Sci. Rep.* **2020**, *10*, 14353. [CrossRef] [PubMed]
46. Saini, D.K.; Impa, S.M.; McCallister, D.; Patil, G.B.; Abidi, N.; Ritchie, G.; Jaconis, S.Y.; Jagadish, K.S.V. High Day and Night Temperatures Impact on Cotton Yield and Quality—Current Status and Future Research Direction. *J. Cotton Res.* **2023**, *6*, 16. [CrossRef]
47. Liu, Q.; Zhang, Z.; Fan, M.; Wang, Q. The Divergent Estimates of Diffuse Radiation Effects on Gross Primary Production of Forest Ecosystems Using Light-use Efficiency Models. *Geophys. Res. Lett.* **2021**, *48*, e2021GL093864. [CrossRef]
48. Jin, Q.; Chachar, M.; Ali, A.; Chachar, Z.; Zhang, P.; Riaz, A.; Ahmed, N.; Chachar, S. Epigenetic Regulation for Heat Stress Adaptation in Plants: New Horizons for Crop Improvement under Climate Change. *Agronomy* **2024**, *14*, 2105. [CrossRef]
49. Bista, M.K.; Kodadinne Narayana, N.; Chakravaram, A.; Pieralisi, B.; Dhillon, J.; Reddy, K.R.; Bheemanahalli, R. Intensifying Heat Stress Impacts Cotton Flowering and Boll Development Efficiency. *BMC Plant Biol.* **2025**, *25*, 984. [CrossRef] [PubMed]
50. Hu, X.; Wong, S.C.; Farquhar, G.D. Coordinated Stomatal, Mesophyll, and Biochemical Functions in Photosynthetic Responses to Heat and Dryness. *Proc. Natl. Acad. Sci. USA* **2026**, *123*, e2605032123. [CrossRef] [PubMed]
51. Behera, S.; Elakkiyaa, T.L.; Sarkar, A.; Dutta, D. Solar-induced Chlorophyll Fluorescence Yield Holds the Potential for Drought Early Warning. *Geophys. Res. Lett.* **2025**, *52*, e2024GL113419. [CrossRef]
52. Chen, J.; Yin, H.; Zhang, K.; Ren, Y.; Zeng, H. Integration of Neural Networks in Brain–Computer Interface Applications: Research Frontiers and Trend Analysis Based on Python. *Eng. Appl. Artif. Intell.* **2025**, *151*, 110654. [CrossRef]
53. Lu, F.; Chen, S.; Hu, Z.; Han, Z.; Alam, K.; Luo, H.; Bi, H.; Chen, J.; Guo, X. Sensitivity and Uncertainties Assessment in Radiative Forcing Due to Aerosol Optical Properties in Diverse Locations in China. *Sci. Total Environ.* **2023**, *860*, 160447. [CrossRef] [PubMed]
54. Dechant, B.; Ryu, Y.; Badgley, G.; Zeng, Y.; Berry, J.A.; Zhang, Y.; Goulas, Y.; Li, Z.; Zhang, Q.; Kang, M.; et al. Canopy Structure Explains the Relationship between Photosynthesis and Sun-Induced Chlorophyll Fluorescence in Crops. *Remote Sens. Environ.* **2020**, *241*, 111733. [CrossRef]
55. Liu, X.; Zhao, H.; Wang, M.; Xia, H.; Wang, D.; Wang, Q.; Song, H. Dust Aerosols Modulate Cloud Radiative Forcing with Surface Cooling and Atmospheric Warming across the Chinese Mainland. *Atmos. Environ.* **2025**, *361*, 121515. [CrossRef]